ACS NANO
Cite This: ACS Nano 2019, 13, 11623−11631
www.acsnano.org

ARTICLE

Lattice Dynamics and Contraction of Energy Bandgap in Photoexcited Semiconducting Boron Nitride Nanotubes

Zhongwen Li,[†] Rui-Juan Xiao,[†] Peng Xu,[†] Chunhui Zhu,[†] Shuaishuai Sun,[†] Dingguo Zheng,[†,‡] Hong Wang,[†,‡] Ming Zhang,[†] Huanfang Tian,[†] Huai-Xin Yang,[†,‡,§] and Jian-Qi Li*[,†,‡,⊥]

[†]Beijing National Laboratory for Condensed Matter Physics, Institute of Physics, Chinese Academy of Sciences, Beijing 100190 China

[‡]School of Physical Sciences, University of Chinese Academy of Sciences, Beijing 100049, China

[§]Yangtze River Delta Physics Research Center Co., Ltd., Liyang, Jiangsu 213300, China

[⊥]Songshan Lake Materials Laboratory, Dongguan, Guangdong 523808, China

Supporting Information

ABSTRACT: **Structural dynamics and changes in electronic structures driven by photoexcited carriers are critical issues in both semiconducting and optoelectronic nanodevices. Herein, a phase diagram for the transient states and relevant dynamic processes in multiwalled boron nitride nanotubes (BNNTs) has been extensively studied for a full reversible cycle after a fs-laser excitation in ultrafast TEMs, and the significant structural features and evolution of electronic natures have been investigated using pulsed electron diffraction and femtosecond-resolved electron energy-loss spectroscopy (EELS). It is revealed that nonthermal anisotropic alterations of the lattice apparently precede the phonon-driven thermal transients along the radial and axial directions. *Ab initio* calculations support these findings and show that electrons excited from the π to π^* orbitals in the BN nanotubes weaken the intralayer bonds while strengthening the interlayer bonds along the radial direction. Importantly, time-resolved EELS measurements show contraction of the energy bandgap after fs-laser excitation associated with nonthermal structural transients. This fact verifies that laser-induced bandgap renormalization in semiconductors can essentially be correlated with both the rapid processes of excited carriers and nonthermal lattice evolution.**

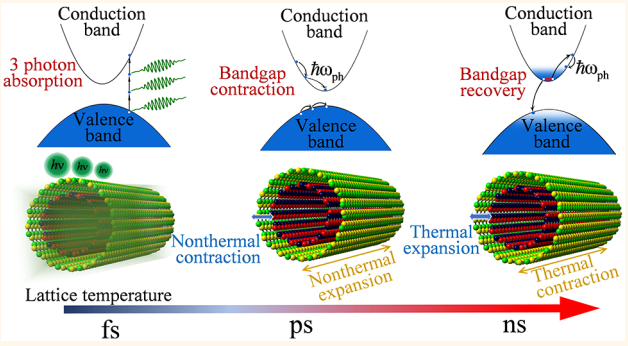

KEYWORDS: *BN nanotubes, nonthermal transient, ultrafast structural dynamics, bandgap renormalization, ultrafast transmission electron microscopy*

Understanding of the structural changes induced by excited electrons in semiconductors and nanomaterials is highly important from both the academic and technological viewpoints, including the fabrication of photoelectric devices using nanomaterials.[1,2] Pump−probe technology, which refers in particular to ultrafast electron diffraction (UED),[3,4] ultrafast electron microscopy (UEM),[5,6] and ultrafast X-ray diffraction (UXRD)[3,7,8] technology, undoubtedly offers considerable advantages in studying these aspects. Related research has been performed into many low-dimensional materials[9−11] and two-dimensional materials.[12−15] Recent research results indicate that carbon nanotubes (CNTs) show a carrier-driven ultrafast lattice response process.[11,16] When CNTs are excited using femtosecond-laser pulses, the CNTs lattices are driven by the carriers, which exhibit ultrafast structural transitions on a picosecond time scale. These processes are driven directly by excited carriers that are generally called nonthermal transients that precede the lattice thermalization driven by phonons. Nonthermal structural change happens immediately after the material is pumped by the femtosecond-pulsed laser.[17] The electrons are excited and the electrostatic potential around the nucleus is modified, then the lattice is deformed without forming the lattice mode vibration. This nonthermal change is different

Received: July 12, 2019
Accepted: September 18, 2019
Published: September 18, 2019

DOI: 10.1021/acsnano.9b05466
ACS Nano 2019, 13, 11623−11631

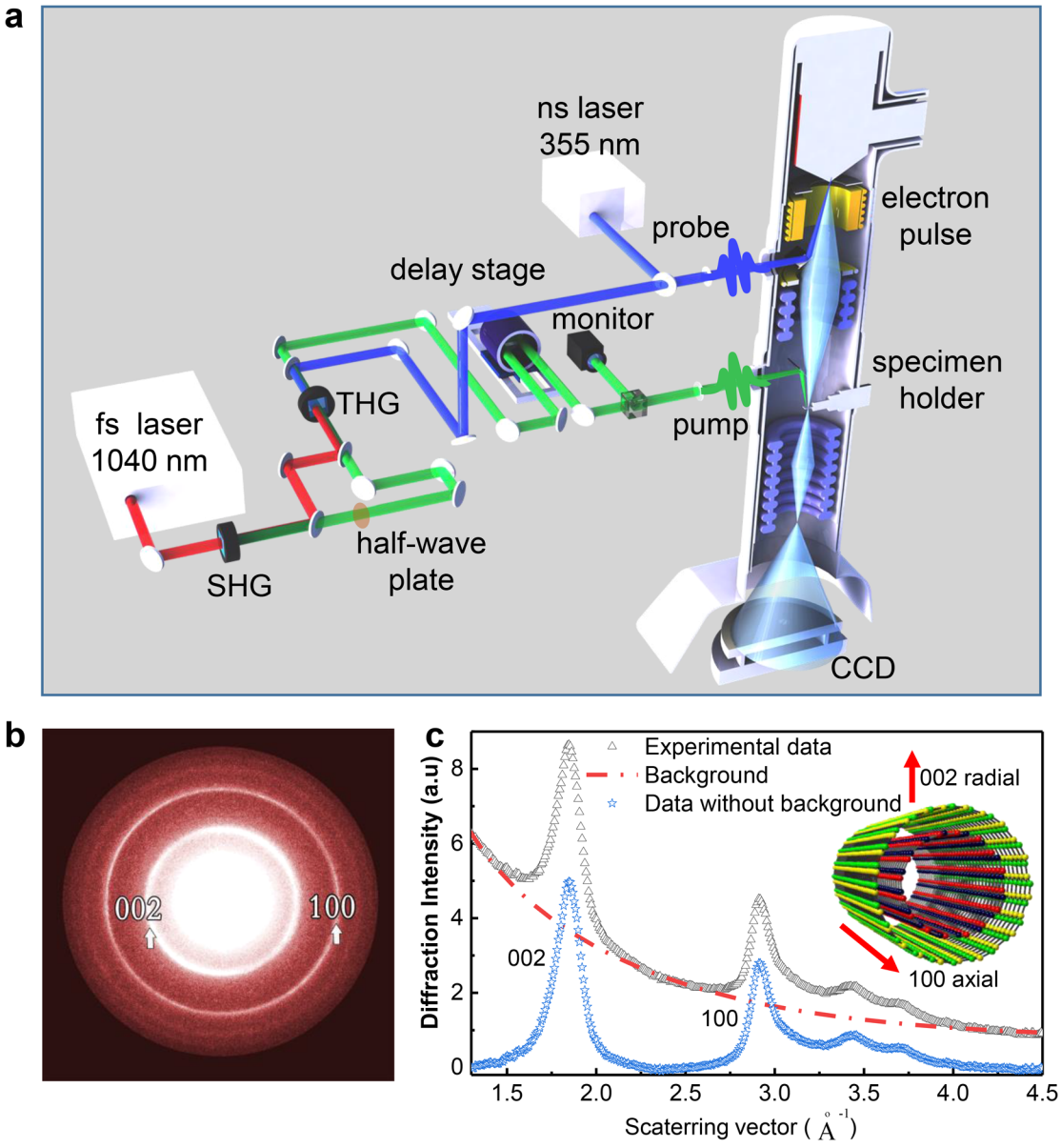

Figure 1. Schematic illustration of ultrafast transmission electron microscope (UTEM) and diffraction pattern with data processing methods for multiwalled boron nitride nanotubes (BNNTs). (a) Pump−probe scheme in the UTEM. (b) Typical pulsed electron diffraction pattern with (002) and (100) crystallographic planes indicated. (c) One-dimensional electron diffraction profiles integrated radially from the 2D diffraction pattern. The inset shows an atomic model of a BNNTs, where the radial and axial directions are indicated using arrows.

from the thermal lattice deformation during which the electrons and lattice are in thermal equilibrium.

Boron nitride nanotubes (BNNTs) with a similar one-dimensional tubular structure[18] have also attracted widespread attention because of their outstanding thermal, mechanical, and chemical properties.[19−22] It is especially noteworthy that BNNTs show good biocompatibility when compared with CNTs and thus have broad application prospects.[23,24] While they have a crystal structure similar to that of the CNTs, the BNNTs band structure is quite different to that of CNTs.[25] The BNNTs energy band gap varies between 5.1 and 5.6 eV, depending on the microstructural layer structures.[26] In our previous article, it was noted that BNNTs can be excited *via* three-photon absorption using a femtosecond-laser with λ = 520 nm and lattice responses arising from thermal phonons associated with electron−phonon coupling and Auger recombination were clearly observed.[27]

This paper describes an extensive study of the lattice alterations and electronic structural changes in BNNTs using time-resolved electron energy-loss spectroscopy (EELS) and diffraction for the excited states. It is shown that the nonthermal structural response, anisotropic lattice transients, occur at different time delays. Importantly, the clear energy bandgap contraction that occurs upon carrier excitation is discussed in correlation with the electronical-driven non-thermal lattice changes.

RESULTS AND DISCUSSION

Structural Dynamics of Photoexcited BNNTs in a Reversible Cycle. Figure 1a shows a schematic diagram of the conceptual design used to develop the UTEMs in our laboratory. An amplified diode-pumped laser system produced the initial laser pulses, which were centered at 1040 nm with a 200 fs duration. Doubling of the pump frequency (520 nm)

DOI: 10.1021/acsnano.9b05466
ACS Nano 2019, 13, 11623−11631

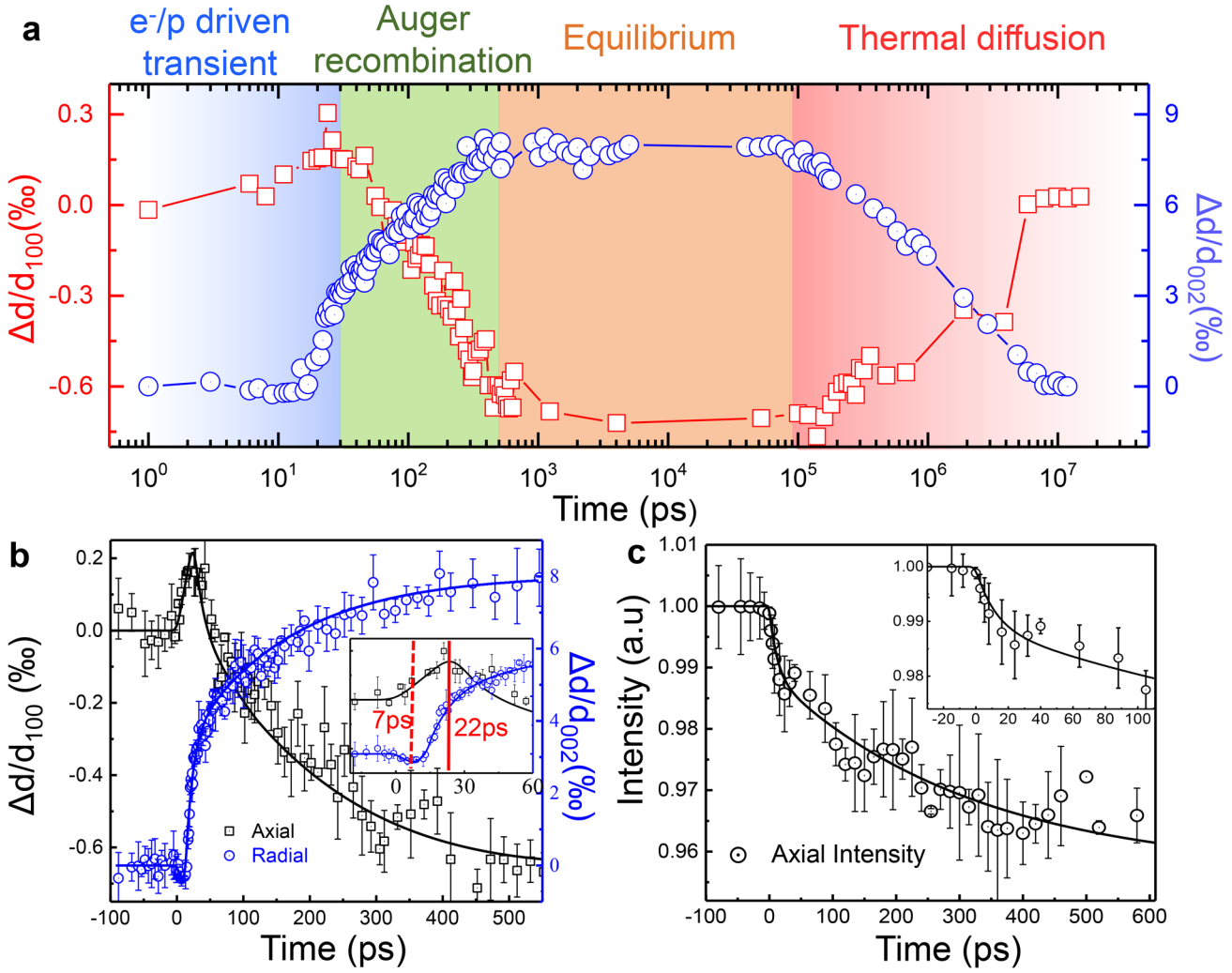

Figure 2. Experimental investigations of ultrafast structural changes in BNNTs upon pulsed femtosecond/nanosecond laser excitation. (a) A diagram showing experimental data and the temporal sequence of dynamics transients in a reversible cycle under a fluence of 50 mJ cm^{-2}. (b) Time-resolved structural data obtained from ultrafast electron diffraction, illustrating the rapid lattice evolution in both the axial and radial directions. The inset shows the anisotropic features of the nonthermal transients, where the maximum responses appear at different times, *i.e.*, at 22 and 7 ps for the axial and radial directions, respectively. (c) Intensity evolution obtained in the axial direction. The inset shows a short time scale.

and tripling of the frequency (347 nm) (or quadrupling at 260 nm) was performed for the probe pulse in ultrafast imaging investigations, while a nanosecond laser system centered at 355 nm with ~10 ns pulse duration was introduced to produce probe pulses in the nanosecond stroboscopic imaging mode. In our experimental study, the UED and femtosecond-resolved EELS experiments on the BNNTs were performed using two home-built UTEMs that were developed based on a JEOL-2000EX microscope and a JEM-2100F microscope equipped with a field-emission electron gun. The fundamental properties of these UTEMs in photoemission mode are illustrated in the Supporting Information (Figures S1 and S2). The femtosecond-scale time resolution in the JEM-2100F-based UTEM is demonstrated directly in the experimental measurements. All photoinduced structural dynamics were initiated using a second 200 fs pump laser (520 nm) with variable fluence of up to 150 mJ cm^{-2}. Actually the BNNTs sample could absorb the pump laser through a three-photon process, and the absorption coefficient and saturated absorption power are discussed in detail in our previous work (ref 27). The results presented in this paper are mostly collected at the pump laser fluence of 50 mJ cm^{-2}, and the absorbed fluence by the sample is estimated to be about 10%.

The UED patterns used in our studies were taken from a specimen area of approximately 5 μm in diameter; a typical example is shown in Figure 1b. These two-dimensional electron diffraction patterns were radially integrated into one-dimensional diffraction profiles for ease of data analysis (see Figure 1c). The diffraction background was then fitted using a three-exponential function and subtracted from the as-acquired 1D diffraction profile. The measurement precision for the lattice change determined by evaluating the peak diffraction profile shift is estimated to be approximately 0.15‰. The inset in Figure 1c depicts the tubular structure of a BNNTs with two distinct chemical bonds, *i.e.*, strong covalent bonds within the (100) intralayer and weak van der Waals bonds within the (002) interlayer.

To study the essential structural features of the transient states upon photoexcitation, we first measured a full reversible cycle *via* stroboscopic imaging using nanosecond- and

DOI: 10.1021/acsnano.9b05466
ACS Nano 2019, 13, 11623−11631

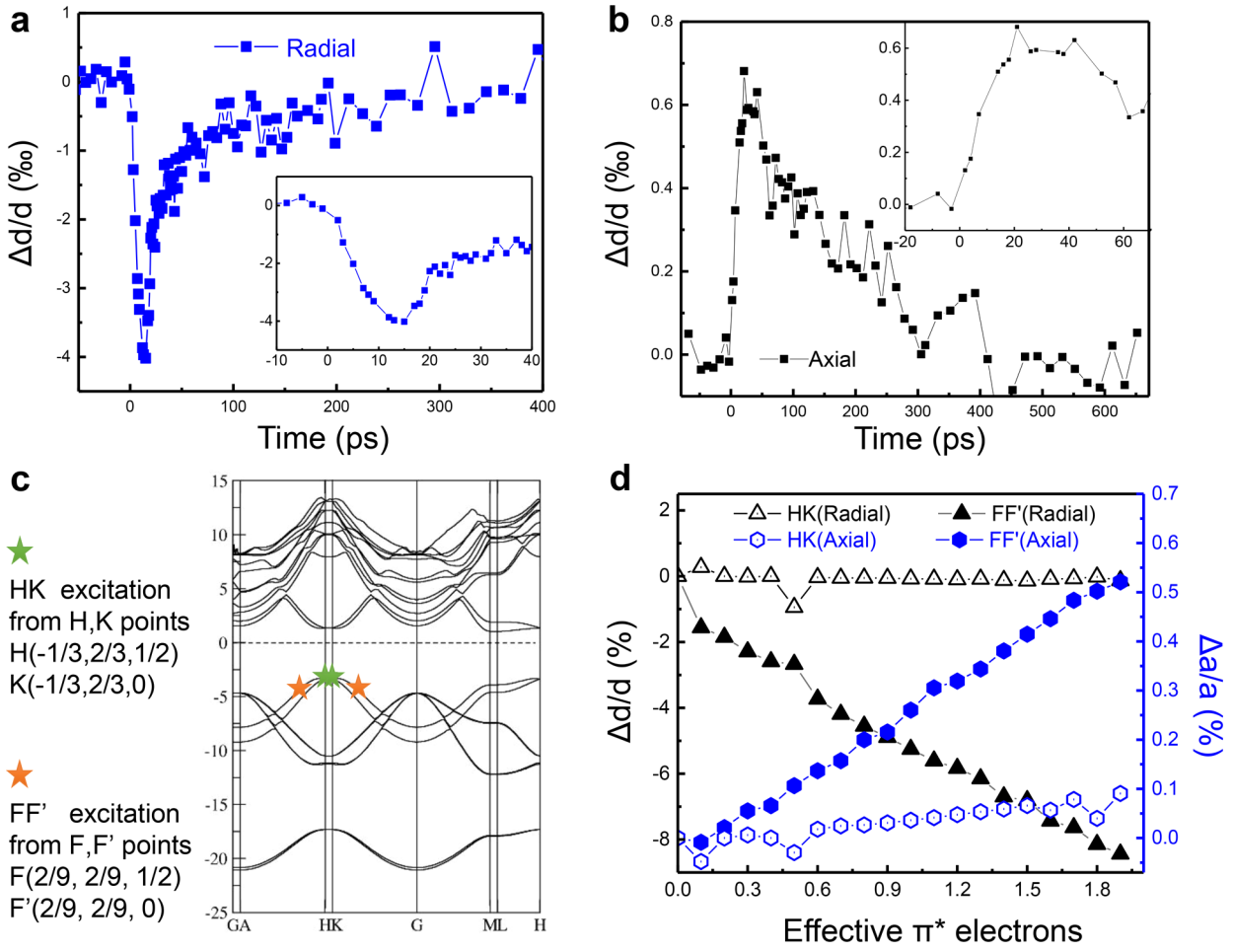

Figure 3. Nonthermal components extracted from Figure 2a after subtraction of the thermal contribution to the total lattice change. (a) Nonthermal process in the radial direction. (b) Nonthermal process in the axial direction. (c) Various selected excitation points at the energy band for the calculations. HK represents the low excitation energy level and FF′ represents the higher excitation energy level. (d) Calculated radial contraction and axial expansion with reference to the excitation point in part c. The radial contraction is more sensitive to changes in the excitation energy.

femtosecond-scale electron diffractions. We obtained a series of electron diffraction patterns at different time delays and then carefully analyzed the structural responses on time scales of up to 30 μs. Figure 2a shows the temporal changes occurring in the interlayer spaces ($\Delta d/d_{002}$) and intralayer spaces ($\Delta d/d_{100}$) of BNNTs under a fluence of 50 mJ cm^{-2}, illustrating a reversible structural evolution cycle after pulsed fs-laser excitation. This demonstrated the presence of a series of notable transient states, including a rapid electron-driven transient process in the early stages, an Auger recombination process with a time scale of hundreds of picoseconds, and hot phonon-driven lattice expansion followed by a thermo-diffusion process on a microsecond time scale. Recognizable thermal-induced lattice changes in BNNTs show up as a small contraction within the (100) sheet and a visible expansion of the (002) interlayer, which shows good agreement with the *in situ* heating measurements.[28] In our previous study, specific lattice dynamic features and transient states in semiconducting BNNTs were discussed briefly in correlation with electron−phonon coupling and Auger recombination.[27] In Figure 2a, we show a diagram and experimental data illustrating the temporal sequence of dynamics transients in a reversible cycle with a time scale of 10 μs. It is notable that the lattice spacing alterations with two distinct slopes are associated with phonon excitation prior to the thermally equilibrated state, which can be understood well based on picosecond-scale electron−phonon scattering and picosecond-to-nanosecond-scale Auger recombination, as commonly discussed in semiconducting systems. It is also found that the reversibility of these dynamic processes in the UTEM observations is strongly determined by the sample's thermal diffusion process and the heat transport between the sample and the UTEM holder. In the present case, the time required for a full dynamic cycle is determined to be ∼10 μs in our experimental measurements of the BNNTs, as illustrated in Figure 2a.

Nonthermal Radial Contraction and Axial Expansion in BNNTs: Experimental Observations. Figure 2b shows the temporal evolution of the lattice spacing for the (002) and (100) planes on a time scale of 500 ps. At time delays greater than 50 ps, it is clearly shown that lattice thermalization yields a visible lattice contraction along the axial direction with expansion along the radial direction. However, we also observed that the radial (002) spacings showed rapid contraction at the early time of t < 7 ps, thus preceding the thermal phonon-driven expansion. Additionally, the axial (100) spacing at t < 20 ps shows rapid expansion followed by clear thermal contraction. In fact, similar dynamic structural features driven by laser-excited electrons (or holes) were also noted in

DOI: 10.1021/acsnano.9b05466
ACS Nano 2019, 13, 11623−11631

CNTs and graphite materials on a time scale of a few picoseconds.[11,16] It was also noted that the different time constants can generally be observed between the axial direction (100) and the radial direction (002), while the anisotropic phenomenon is believed to be correlated with the layered structure and the different natures of the intralayer and interlayer chemical bonds. To analyze the fundamental properties of these lattice changes in the nonthermal process, the experimental data of the (100) peak intensities were also measured and are shown in Figure 2c, where the temporal changes in diffraction intensity are mainly related to lattice thermalization and carrier-phonon scattering.[29] Careful analysis of the data in Figure 2c reveals that two dynamic processes arise in the intensity change because of carrier-phonon scattering: a fast process with a time constant of approximately 15 ps can be explained well by electron−phonon coupling, while the slow process with a time constant of approximately 180 ps is caused by the Auger recombination[17,27] that often occurs in association with carrier recombination in excited semiconductors. Using these experimental data, we can also discuss the temperature changes based on reported data for thermal expansion of BNNTs,[28] where the lattice temperature is estimated to be approximately 500 K at a time delay of 10 ns but cools down to room temperature after approximately 10 μs. By subtracting the thermal phonon-driven component from the lattice changes shown in Figure 2b, the electron-driven component for the nonthermal transient can be obtained as shown in Figure 3, in which the time for the increase in lattice spacing can be determined to be 25 ± 3 ps along the axial direction, while the amplitude peak is 0.4‰. Similarly, the nonthermal contraction time in the radial direction is determined to be 12 ± 3 ps and the amplitude peak can be determined to be 6‰. The structural changes along both the axial and radial directions follow double exponential decay processes after they reach their peaks.

According to the time-dependent data of diffraction intensity, we can calculate the temperature for lattice by Debye−Waller effects, the phonon-induced thermal process has been well fitted by the biexponential function.[27] After deducting the contribution of phonons to the experimental data, the nonthermal changes can be obtained for BNNTs materials. The anisotropic properties of the nonthermal structural transients driven by the excited carriers represent another critical issue in our investigations, as illustrated in Figure 3a,b. The intralayer and interlayer lattice responses show obvious differences in terms of both lattice changes and their temporal dependences after femtosecond laser excitation, and visible contraction along the [002] axis and expansion along the [100] axis are commonly observed on a picosecond time scale. This clearly demonstrates the presence of anisotropic electron and lattice processes in the excited nanotubes before lattice thermalization. It is known that the nonthermal responses are essentially correlated with the nature of the excited state, particularly in the case of the effects of the carrier cooling dynamics in the excited conduction bands. In Figure 3c,d, we present a theoretical analysis of the lattice effects of charge carriers in the excited state. Two typical excitations, happened at F(F′) or H(K) points in the Brillouin zone, respectively, are discussed in present investigations. The former excitation is selected according to the maximum energy providing by the three-photon process. At F(F′), the energy absorbed by the electron hopping from the top of the occupied level to the conduction band is close to the energy given by three photons (~7.2 eV). The excitation at H(K) simulates the relaxation state for excited electrons coming back to the lowest energy levels in the conduction band. The effects of above excitation processes on the lattice along the radial and axial of BNNTs are evaluated through DFT simulations, as shown in Figure 3d, it is recognizable that the excitation at F(F′) point yields relatively large interlayer contraction leading to the lattice decrease in the radial direction and increase in the axial direction of BNNTs. After the excited electrons relax to the bottom of the conduction band, (the H(K) point), the lattice of BNNTs will not change obviously, corresponding to the relatively longer time constant for intrasheet nonthermal changes in the transient state, as observed experimentally. In fact, this initial compression for nonthermal transients in graphite was also noted in ultrafast structural measurements,[29−31] in which cooperative lattice motion dictated by the potential of the excited carriers is guided by the out-of-equilibrium electronic structural change after femtosecond-scale excitation as also discussed for the TiO_2 semiconductor in ref 32, and the excited carriers could strongly affect the lattice distances. In general, this dynamic process is essentially driven by electronic changes on scales ranging from femtoseconds to a few picoseconds, followed by clear decay associated with carrier removal.

Nonthermal Radical Contraction and Axial Expansion in BNNTs: Theoretical Verification. To understand the lattice dynamics driven by these photoexcited electrons, we have investigated the effects of laser pulses on the electronic structure and chemical bonding in BN nanotubes extensively using density functional theory (DFT) calculations.[33−35] The photoexcitation effect is simulated using a fixed partial electron occupancy, where a fraction of the electrons from the highest occupied state are moved to the lowest unoccupied state. Figure 4a depicts the changes in the BNNTs lattice spacings as a function of the excited electrons, in which axial expansion (red circles) and radial contraction (black squares) are clearly revealed upon an increase in the excitation level. In the point of microscopic mechanism, our analysis also show that the B−N bond lengths shows visible variations at different excitation state after the femtosecond-pulsed laser excitation, e.g., the B−N bond lengths obtained from simulations are 1.454 (in the axial direction)/1.450(in the radial direction) Å and 1.459 (in the axial direction)/1.452 (in the radial direction) Å in the ground state and the state with one electron excited to π^*, respectively. These types of lattice alterations are essentially caused by the various electron occupations in the excited states. At an excitation level of one electron (from the π to π^* orbitals), the radial direction contracts by 6% while the axial direction of the nanotube expands by only approximately 4‰.

Figure 4b shows the charge density ρ difference between the ground and excited states of a single-walled BN nanotube, in which the charge densities of the π-bond on the BN rings decrease (purple isosurface), while those of the σ-bond (yellow isosurface) increase. The charge density changes upon electronic excitation for these two bond types show the opposite behavior to that of the charge redistributions. The depopulation of electrons (in the band picture from the π bands to the unoccupied π^* bands) in the π-bond upon laser excitation weakens the intralayer B−N bonds, which explains the experimentally observed expansion in the (100) axial direction. In contrast, the gain in the charge density of the σ-bond perpendicular to the axial direction strengthens the interlayer interaction while reducing the interlayer spacing, as

DOI: 10.1021/acsnano.9b05466
ACS Nano 2019, 13, 11623−11631

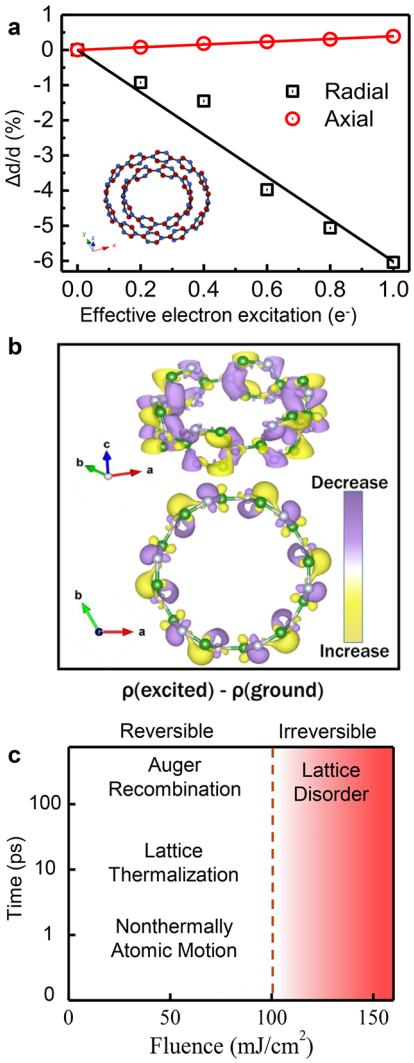

Figure 4. Theoretical investigations and laser fluence dependence of structural changes in BNNTs. (a) Calculated lattice changes for double-walled BNNTs as a function of the effective electron excitation, illustrating the essentially different features driven by π to π^* excitation. The inset shows an atomic model of a double-walled BNNTs. (b) Change in electron density between the ground and excited states (following electron excitation from π into π^*). The charge density decreases in the axial direction (yellow isosurfaces) but increases in the B−N bonds along the radial direction (purple isosurfaces). (c) Regime diagram summarizing the time scale and fluence dependences of the structural changes in BNNTs upon femtosecond-pulsed laser excitation. The laser fluence ranges from 0 to 150 mJ cm^{-2}.

indicated by the experimentally observed radial contraction of BNNTs under photoexcitation. Figure 4c shows the fluence dependence of the BNNTs lattice dynamics, with a determined fluence threshold of ~100 mJ cm^{-2}; above this threshold, lattice defects and damage to the tubular structure commonly occur in the lattice; below the threshold, the BNNTs undergo well-defined reversible dynamic processes involving rapid nonthermal responses, electron−phonon thermalization, and Auger recombination.

Figure S3 shows static EELS results measured from BN tube samples with well-defined tubular crystal structures. The distinct features observed in the spectrum are similar to previously reported data for BNNTs;[26] the in-plane plasmon peak is found near 7.5 eV, while the peak at 25 eV is known to be the oscillation of the bulk plasmon. It is noted that surface losses and Cherenkov radiation often produce clear contributions in the low-loss region, so the energy bandgap information cannot be extracted correctly using the conventional Kramers−Kronig transformation.[36] To improve the numerical efficiency and stability of the solution, we use a method reported in ref 37 based on the Kroger model; the dielectric function obtained and the theoretical simulation data shown in Figure 3c agree well with the experimental data, as also discussed in the Supporting Information. The bandgap energy is well-known to be visibly dependent on the tubular structural features, including the structural layers and diameter of the nanotubes. TEM observations have shown that the BNNTs in our sample often contain 30−40 structural layers, while the bandgaps were measured experimentally to be approximately 4.9 eV based on the Kroger model.

To investigate the changes in the electron structure associated with the charge carrier processes in excited BNNTs, we first investigate the time-resolved changes in the typical plasmon peaks obtained for time delays ranging from −10 to 100 ps. It is commonly noted that the presence of redshifts can be observed in the π plasmon resonances after femtosecond-pulsed laser excitation.

Figure 5a shows a series of EELS results obtained at various time delays for the peak at approximately 7.5 eV arising from the $\pi-\pi^*$ transitions; it is observed that a visible redshift appears for this valence excitation peak, indicating a reduction in the energy bandgap upon femtosecond-laser excitation. A peak feature is also noted at a shoulder of 6.0 eV on the low energy side of the plasmon peaks of the BNNTs; this feature is also a $\pi-\pi^*$ transition[38] and is temporally sensitive with regard to the carrier process in the excited state. Theoretical calculations showed that the two peaks above can be assigned to the $\pi-\pi^*$ transition at the P and Q points of the two-dimensional band structure of h-BN,[39] respectively.

To investigate the electronic changes and the redshift of the π-plasmon peak upon femtosecond-laser excitation systematically, we have obtained the real (ε_1) and imaginary (ε_2) parts of the dielectric function that were derived from the loss function using the Kroger model, as shown in Figure 5 and illustrated in the Supporting Information. The imaginary part of the dielectric function ε_2 in Figure 5b from the time-resolved EELS data obtained at a time delay of 8.7 ps, in which the plasmon peak corresponds to the $\pi-\pi^*$ transition, shows a visible shift toward the lower energy. In contrast, the $\pi + \sigma$ plasmon only shows a limited change to be obtained for the excited states. To enable comparison, the dielectric function (ε) obtained from the EELS spectra before the optical pulse (t = −10 ps) is also shown. A 960 meV red shift is clearly demonstrated at the peak position, corresponding to alteration of the bandgap energy.

Additionally, the time-resolved diffraction technique[4−6] is well-known to provide direct access to the dynamics of structural alterations driven by both electrons and phonons, as discussed above (Figure 2).[37,40] Therefore, we also present the nonthermal evolution of the BNNTs interlayer spacing obtained by UED at a similar fluence for the same sample, *i.e.*, 50 mJ cm^{-2}, where interlayer compression (see Figure 2) appears on a similar time scale to the reduction in the energy bandgap in the excited state and the π plasmon is out of equilibrium. In Figure 5c (bottom panel), we present experimental data obtained from a series of time-resolved

DOI: 10.1021/acsnano.9b05466
ACS Nano 2019, 13, 11623−11631

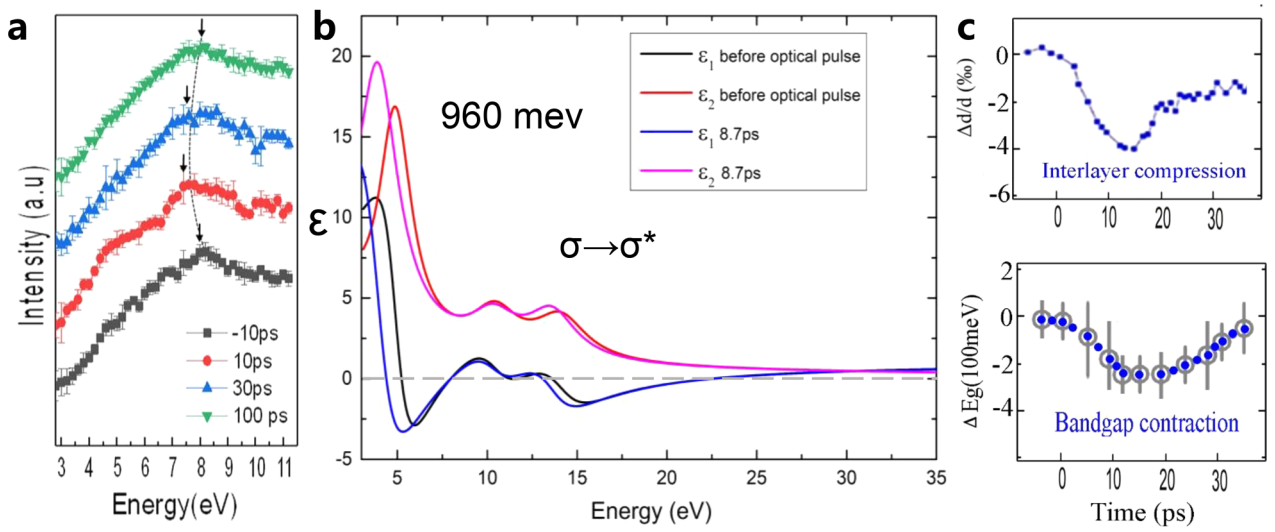

Figure 5. Time-resolved analysis of electronic structural changes in BNNTs. (a) The π-plasmon peaks shift with the time delays, illustrating the valence excitation features of the $\pi-\pi^*$ transitions upon fs-laser excitation. (b) Dielectric function of the BNNTs showing the real and imaginary parts derived from the loss function, which yields a clear contraction of the energy bandgap at an excited state. (c) Change in the interlayer spacing and contraction of the energy bandgap as measured from −10 to 40 ps, showing the cooperative evolution of the bandgap and the nonthermal structural transient in BNNTs.

EELS measurements at various time delays. Recognizable cooperative alterations in the interlayer compression (up panel) and bandgap contraction appear on the picosecond time scale. In semiconductors, the laser-induced energy bandgap renormalization has been theoretically discussed and experimentally investigated as a critical issue using a variety of materials.[41−43] It is commonly noted that bandgap reduction upon laser excitation could obviously affect both charge carrier diffusion and the fundamental nature of energy transport from photoexcited regions. Our study clearly shows that laser-induced bandgap renormalization appears to be essentially related not only to the excited carrier processes but also to nonthermal lattice changes in semiconducting materials.[41,42]

CONCLUSION

In summary, UED and time-resolved EELS measurements in UTEMs have been used to study the ultrafast dynamics of the crystal lattice and the electronic structure in semiconducting BNNTs. In particular, the nonthermal lattice alterations and energy bandgap contractions upon femtosecond-pulsed laser excitation were extensively investigated and all mainly show correlation with the ultrafast processes of the excited π electrons. Our experimental results also showed anisotropic changes in the nonthermal structural transition along the radial and axial directions in the BNNTs because of the anisotropic bond nature of these tubular structures. Theoretical calculations supported these findings and revealed that electrons excited from the π to π^* orbitals in BNNTs weaken the intralayer bonds while strengthening the interlayer bonds along the radial direction. Importantly, our measurements clearly demonstrate that the nonthermal interlayer compression and bandgap contraction appear cooperatively in BNNTs prior to the thermal phonon-driven structural transient. This observation verifies that the laser-induced bandgap renormalization that is commonly discussed in semiconductors can essentially be affected by nonthermal lattice transients associated with the ultrafast transients of excited carriers.

EXPERIMENTAL SECTION

UTEM Instruments. In the present study, two UTEMs have been used in the time-resolved experimental measurements: spatiotemporal resolution for the UTEM (the first generation) developed based on a JEOL-2000EX microscope has been well addressed in our previous publications. Its time resolution in investigations of lattice dynamics is better than 1 ps.[28,44] Moreover, this UTEM is equipped with both femtosecond and nanosecond pulsed laser systems, which allow us to perform stroboscopic observations on lattice dynamics at high temporal resolution as well as on lattice evolution in a full dynamic cycle with nanosecond temporal resolution as illustrated in Figure 1 and Figure 2.

Another UTEM is a newly developed one based on a JEM-2100F (JEOL Inc.) electron microscope which is equipped with the field-emission electron gun operated at 200 kV (with a W/ZrO_2 cathode 120 nm in diameter). Figure S1 shows a photograph of this UTEM at our laboratory, together with a single-electron diffraction pattern for the Ag single crystal and an electron energy loss spectrum. This UTEM driven by a femtosecond-pulsed laser system shows a time resolution of ∼400 fs as measured using electron energy loss spectroscopy (schematic in Figure S2), which allows us to perform analysis of structural transients, lattice dynamics, and rapid changes of the electronic structures.

TEM Specimen Preparation. The BNNTs samples used here have been well characterized in our previous publications.[20,45] The BNNTs samples have average diameters of 40 ± 10 nm and typical lengths of 10 μm. For the ultrafast transmission electron microscope (UTEM) experiments, BNNTs were dispersed in ethanol using an ultrasonicator and a few droplets of this suspension were cast onto a 2000-mesh copper grid. A second 400-mesh copper grid was placed on top of the 2000-mesh grid to sandwich the specimens and enhance their mechanical stability during laser excitation. As a result, the specimen consisted of a woven network of nanotubes with random orientation.

EELS Measurements. The energy width for the photoemission pulsed electron is about 0.65 eV as measured for the EELS zero-loss peak; it is comparable to that obtained in thermal-mode operation of the conventional TEM. Herein our experiments were performed at repetition rates between 100 kHz and 500 kHz, and no difference in the EEL spectra or the temporal behavior was observed, signifying a complete recovery of electronic structure changes between subsequent pulses. The temporal and energy resolutions often depend

DOI: 10.1021/acsnano.9b05466
ACS Nano 2019, 13, 11623−11631

significantly beam intensity due to the appearance of the space-charge effects.

Time resolved EELS data were recorded in the UTEM. The electron pulses were accelerated in the TEM column and dispersed after transmission through the sample in order to provide the energy loss spectrum of the tubular material. The diameter of the converged electron beam (~150 nm) was sufficiently large to cover a large enough amount of randomly oriented BN nanotubes. The collection angles were approximately 5 mrad. The time trace was fitted with the combination of an exponential decay and an exponential increase as reported in the previous literature.

EELS Analysis. The experimental data of electron energy loss intensity is processed with the Fourier log deconvolution method to remove the zero loss peak and multiple scattering effect. Single scattering probability is obtained from the data recorded before and after the optical pulse.[36] While the dielectric permittivity of the material is conventionally obtained from the single scattering probability by Kramers–Kronig transformation,[36] the surface loss and Cherenkov radiation are not considered by this method, and thus the band gap information in the low loss region cannot be extracted correctly by this method.[46] By application of the Kroger mode,[40] Qingping Meng *et al.* raise a method to extract the correct dielectric function from VEELS data.[37] To improve the numerical efficiency and stability of the solution, we use a different method to extract the dielectric function from ref 37. First, we carry out Kramers–Kronig transform to the single scattering probability and obtain the real and imaginary parts of the dielectric permittivity. The same as ref 37, we use it as an initial guess of the real dielectric function of the material. We use multiple Lorentz oscillators to fit the real and imaginary part of this dielectric function and obtain the parameters of the Lorentz oscillators which will be used later. Similar to ref 37, we use the Kroger model to calculate the single scattering probability and thus take the effect of the surface loss and Cherenkov radiation into consideration. Instead of solving for the dielectric function directly, we solve the correct parameters of the Lorentz oscillators by fitting the calculated single scattering probability with the Kroger model and dielectric constants determined by the parameters of the Lorentz oscillators to the relevant probability obtained from the experimental data in the least-squares sense. The correct parameters of the Lorentz oscillators are obtained by applying the oscillator parameters obtained earlier by Kramers–Kronig transform as initial data during fitting. After we obtain the correct parameters of the Lorentz oscillators, the real and imaginary part of the dielectric permittivity are calculated for analysis of structural features as observed in time-resolved experimental EELS measurements.

DFT Simulations. The Vienna *ab initio* simulation package (VASP)[33] for the projector augmented-wave (PAW) approach[34] was adopted for our DFT calculations. The exchange–correlation function is described using the generalized gradient approximation in the parametrization of the Perdew, Burke, and Ernzerhof (PBE) functional.[35] The cutoffs of the wave function and charge density are 600 and 900 eV, respectively. The single-walled BN nanotube, as used for the theoretical analysis of intralayer atom motions, is modeled using a unit cell with 12 boron atoms and 12 nitrogen atoms in a 20.088 × 20.088 × 2.520 $Å^3$ hexagonal lattice, where sufficient vacuum is introduced around the nanotube to avoid interactions among neighboring images because of the translational periodicity. In this model, the unit cells are fully optimized using a k-mesh with a density of one point per ~0.03 $Å^{-3}$ to obtain the change of the nanotube along the axial and radial directions caused by electronic excitation. For the relaxation of all the cases, the forces exerted by each of the atoms are well converged below 0.01 eV $Å^{-1}$, and the total energies are converged below 10^{-5} eV per cell.

ASSOCIATED CONTENT

Supporting Information

The Supporting Information is available free of charge on the ACS Publications website at DOI: 10.1021/acsnano.9b05466.

Photograph of the UTEM microscope developed based on a JEM-2100F TEM, electron energy-loss spectra taken from carbon nanotubes at different delay times, excitation wavelength is 520 nm and F = 50 mJ cm^{-2}, and EELS data of BN nanotube with diameters ranging from 30 to 40 nm (PDF)

AUTHOR INFORMATION

Corresponding Author

*E-mail: ljq@aphy.iphy.ac.cn.

ORCID

Zhongwen Li: 0000-0001-9294-9288
Shuaishuai Sun: 0000-0002-9363-3901
Jian-Qi Li: 0000-0002-4808-6347

Author Contributions

J.L. conceived and designed the experiments; Z.L., C.Z., S.S., D.Z, and H.W. performed the experiments; Z.L., R.X., P.X., H.T., and H.Y. analyzed the data; Z.L. wrote the paper with contributions from all coauthors.

Notes

The authors declare no competing financial interest.

ACKNOWLEDGMENTS

This work was supported by the National Key Research and Development Program of China under Grant Nos. 2016YFA0300303, 2017YFA0504703, 2017YFA0302904, and 2017YFA0303000, the National Basic Research Program of China under Grant No. 2015CB921304, the National Natural Science Foundation of China under Grant Nos. 11774391, 11774403, and 11804381, the Strategic Priority Research Program (B) of the Chinese Academy of Sciences under Grant Nos. XDB25000000 and XDB07020000, the Scientific Instrument Developing Project of the Chinese Academy of Sciences under Grant No. ZDKYYQ20170002, and the Postdoctoral Innovation Talent Support Program of China (Grant No. BX20180351). We thank David MacDonald, MSc, from Liwen Bianji, Edanz Editing China (www.liwenbianji.cn/ac), for editing the English text of a draft of this manuscript. We also thank Siyuan Huang for assisting with the data analysis.

REFERENCES

(1) Xia, Y.; Yang, P.; Sun, Y.; Wu, Y.; Mayers, B.; Gates, B.; Yin, Y.; Kim, F.; Yan, H. One-Dimensional Nanostructures: Synthesis, Characterization, and Applications. *Adv. Mater.* **2003**, *15*, 353–389.
(2) Srivastava, A.; Marulanda, J. M.; Xu, Y.; Sharma, A. Carbon-Based Electronics. *Nat. Nanotechnol.* **2007**, *2*, 605.
(3) Chergui, M.; Zewail, A. H. Electron and X-Ray Methods of Ultrafast Structural Dynamics: Advances and Applications. *ChemPhysChem* **2009**, *10*, 28–43.
(4) Sciaini, G.; Miller, R. J. D. Femtosecond Electron Diffraction: Heralding the Era of Atomically Resolved Dynamics. *Rep. Prog. Phys.* **2011**, *74*, 096101.
(5) Zewail, A. H. Four-Dimensional Electron Microscopy. *Science* **2010**, *328*, 187–193.
(6) Vanacore, G. M.; Fitzpatrick, A. W. P.; Zewail, A. H. Four-Dimensional Electron Microscopy: Ultrafast Imaging, Diffraction and Spectroscopy in Materials Science and Biology. *Nano Today* **2016**, *11*, 228–249.
(7) Bargheer, M.; Zhavoronkov, N.; Woerner, M.; Elsaesser, T. Recent Progress in Ultrafast X-Ray Diffraction. *ChemPhysChem* **2006**, *7*, 783–792.

DOI: 10.1021/acsnano.9b05466
ACS Nano 2019, 13, 11623–11631

(8) Lindenberg, A. M.; Johnson, S. L.; Reis, D. A. Visualization of Atomic-Scale Motions in Materials *via* Femtosecond X-Ray Scattering Techniques. *Annu. Rev. Mater. Res.* **2017**, *47*, 425−449.
(9) Yang, D.-S.; Lao, C.; Zewail, A. H. 4D Electron Diffraction Reveals Correlated Unidirectional Behavior in Zinc Oxide Nanowires. *Science* **2008**, *321*, 1660−1664.
(10) Muller, M.; Paarmann, A.; Ernstorfer, R. Femtosecond Electrons Probing Currents and Atomic Structure in Nanomaterials. *Nat. Commun.* **2014**, *5*, 5292.
(11) Sun, S.; Li, Z.; Li, Z. A.; Xiao, R.; Zhang, M.; Tian, H.; Yang, H.; Li, J. Cooperative Inter- and Intra-Layer Lattice Dynamics of Photoexcited Multi-Walled Carbon Nanotubes Studied by Ultrafast Electron Diffraction. *Nanoscale* **2018**, *10*, 7465−7471.
(12) Sun, S.; Wei, L.; Li, Z.; Cao, G.; Liu, Y.; Lu, W. J.; Sun, Y. P.; Tian, H.; Yang, H.; Li, J. Direct Observation of an Optically Induced Charge Density Wave Transition in1T−$TaSe_2$. *Phys. Rev. B: Condens. Matter Mater. Phys.* **2015**, *92*, 224303.
(13) Wei, L.; Sun, S.; Guo, C.; Li, Z.; Sun, K.; Liu, Y.; Lu, W.; Sun, Y.; Tian, H.; Yang, H.; Li, J. Dynamic Diffraction Effects and Coherent Breathing Oscillations in Ultrafast Electron Diffraction in Layered 1T-TaSeTe. *Struct. Dyn.* **2017**, *4*, 044012.
(14) Mannebach, E. M.; Li, R.; Duerloo, K. A.; Nyby, C.; Zalden, P.; Vecchione, T.; Ernst, F.; Reid, A. H.; Chase, T.; Shen, X.; Weathersby, S.; Hast, C.; Hettel, R.; Coffee, R.; Hartmann, N.; Fry, A. R.; Yu, Y.; Cao, L.; Heinz, T. F.; Reed, E. J.; et al. Dynamic Structural Response and Deformations of Monolayer MoS_2 Visualized by Femtosecond Electron Diffraction. *Nano Lett.* **2015**, *15*, 6889−6895.
(15) Mannebach, E. M.; Nyby, C.; Ernst, F.; Zhou, Y.; Tolsma, J.; Li, Y.; Sher, M. J.; Tung, I. C.; Zhou, H.; Zhang, Q.; Seyler, K. L.; Clark, G.; Lin, Y.; Zhu, D.; Glownia, J. M.; Kozina, M. E.; Song, S.; Nelson, S.; Mehta, A.; Yu, Y.; et al. Dynamic Optical Tuning of Interlayer Interactions in the Transition Metal Dichalcogenides. *Nano Lett.* **2017**, *17*, 7761−7766.
(16) Vanacore, G. M.; van der Veen, R. M.; Zewail, A. H. Origin of Axial and Radial Expansions in Carbon Nanotubes Revealed by Ultrafast Diffraction and Spectroscopy. *ACS Nano* **2015**, *9*, 1721−1729.
(17) Sundaram, S. K.; Mazur, E. Inducing and Probing Non-Thermal Transitions in Semiconductors Using Femtosecond Laser Pulses. *Nat. Mater.* **2002**, *1*, 217.
(18) Golberg, D.; Bando, Y.; Tang, C. C.; Zhi, C. Y. Boron Nitride Nanotubes. *Adv. Mater.* **2007**, *19*, 2413−2432.
(19) Zhi, C.; Bando, Y.; Tang, C.; Xie, R.; Sekiguchi, T.; Golberg, D. Perfectly Dissolved Boron Nitride Nanotubes Due to Polymer Wrapping. *J. Am. Chem. Soc.* **2005**, *127*, 15996−15997.
(20) Zhi, C.; Bando, Y.; Tan, C.; Golberg, D. Effective Precursor for High Yield Synthesis of Pure BN Nanotubes. *Solid State Commun.* **2005**, *135*, 67−70.
(21) Li, L. H.; Chen, Y. Superhydrophobic Properties of Nonaligned Boron Nitride Nanotube Films. *Langmuir* **2010**, *26*, 5135−5140.
(22) Wang, J.; Lee, C. H.; Yap, Y. K. Recent Advancements in Boron Nitride Nanotubes. *Nanoscale* **2010**, *2*, 2028−2034.
(23) Lee, C. H.; Zhang, D.; Yap, Y. K. Functionalization, Dispersion, and Cutting of Boron Nitride Nanotubes in Water. *J. Phys. Chem. C* **2012**, *116*, 1798−1804.
(24) Ciofani, G.; Danti, S.; Genchi, G. G.; Mazzolai, B.; Mattoli, V. Boron Nitride Nanotubes: Biocompatibility and Potential Spill-over in Nanomedicine. *Small* **2013**, *9*, 1672−1685.
(25) Cohen, M. L.; Zettl, A. The Physics of Boron Nitride Nanotubes. *Phys. Today* **2010**, *63*, 34−38.
(26) Terauchi, M.; Tanaka, M.; Matsumoto, T.; Saito, Y. Electron Energy-Loss Spectroscopy Study of the Electronic Structure of Boron Nitride Nanotubes. *J. Electron Microsc.* **1998**, *47*, 319−324.
(27) Li, Z.; Sun, S.; Li, Z. A.; Zhang, M.; Cao, G.; Tian, H.; Yang, H.; Li, J. Ultrafast Structural Dynamics of Boron Nitride Nanotubes Studied Using Transmitted Electrons. *Nanoscale* **2017**, *9*, 13313−13319.
(28) Li, Z.; Li, Z. A.; Sun, S.; Zheng, D.; Wang, H.; Tian, H.; Yang, H.; Bai, X.; Li, J. Direct Observation of Inner-Layer Inward Contractions of Multiwalled Boron Nitride Nanotubes Upon *In Situ* Heating. *Nanomaterials* **2018**, *8*, 86.
(29) Schäfer, S.; Liang, W.; Zewail, A. H. Primary Structural Dynamics in Graphite. *New J. Phys.* **2011**, *13*, 063030.
(30) Carbone, F.; Baum, P.; Rudolf, P.; Zewail, A. H. Structural Preablation Dynamics of Graphite Observed by Ultrafast Electron Crystallography. *Phys. Rev. Lett.* **2008**, *100*, 035501.
(31) Raman, R.; Murooka, Y.; Ruan, C.-Y.; Yang, T.; Berber, S.; Tománek, D. Direct Observation of Optically Induced Transient Structures in Graphite Using Ultrafast Electron Crystallography. *Phys. Rev. Lett.* **2008**, *101*, 077401.
(32) Bothschafter, E. M.; Paarmann, A.; Zijlstra, E. S.; Karpowicz, N.; Garcia, M. E.; Kienberger, R.; Ernstorfer, R. Ultrafast Evolution of the Excited-State Potential Energy Surface of TiO_2 Single Crystals Induced by Carrier Cooling. *Phys. Rev. Lett.* **2013**, *110*, 067402.
(33) Blöchl, P. E. Projector Augmented-Wave Method. *Phys. Rev. B: Condens. Matter Mater. Phys.* **1994**, *50*, 17953.
(34) Kresse, G.; Furthmüller, J. Efficiency of *Ab Initio* Total Energy Calculations for Metals and Semiconductors Using a Plane-Wave Basis Set. *Comput. Mater. Sci.* **1996**, *6*, 15−50.
(35) Perdew, J. P.; Burke, K.; Ernzerhof, M. Generalized Gradient Approximation Made Simple. *Phys. Rev. Lett.* **1996**, *77*, 3865.
(36) Egerton, R. F. Kramers-Kronig Transformation. In *Electron Energy-Loss Spectroscopy in the Electron Microscope*; Plenum Press: New York, 1986; pp 367−368.
(37) Meng, Q.; Wu, L.; Xin, H. L.; Zhu, Y. Retrieving the Energy-Loss Function from Valence Electron Energy-Loss Spectrum: Separation of Bulk-, Surface-Losses and Cherenkov Radiation. *Ultramicroscopy* **2018**, *194*, 175−181.
(38) Fuentes, G. G.; Borowiak-Palen, E.; Pichler, T.; Liu, X.; Graff, A.; Behr, G.; Kalenczuk, R. J.; Knupfer, M.; Fink, J. Electronic Structure of Multiwall Boron Nitride Nanotubes. *Phys. Rev. B: Condens. Matter Mater. Phys.* **2003**, *67*, 035429.
(39) Zunger, A.; Katzir, A.; Halperin, A. Optical Properties of Hexagonal Boron Nitride. *Phys. Rev. B* **1976**, *13*, 5560.
(40) Kröger, E. Transition Radiation, Cerenkov Radiation and Energy Losses of Relativistic Charged Particles Traversing Thin Foils at Oblique Incidence. *Eur. Phys. J. A* **1970**, *235*, 403−421.
(41) Kalt, H.; Rinker, M. Band-Gap Renormalization in Semiconductors with Multiple Inequivalent Valleys. *Phys. Rev. B: Condens. Matter Mater. Phys.* **1992**, *45*, 1139.
(42) Zimmermann, R. *Many-Particle Theory of Highly Excited Semiconductors*; Teubner: Leipzig, Germany, 1988.
(43) Roth, S.; Crepaldi, A.; Puppin, M.; Gatti, G.; Bugini, D.; Grimaldi, I.; Barrilot, T. R.; Arrell, C. A.; Frassetto, F.; Poletto, L.; Chergui, M.; Marini, A.; Grioni, M. Photocarrier-Induced Band-Gap Renormalization and Ultrafast Charge Dynamics in Black Phosphorus. *2D Mater.* **2019**, *6*, 031001.
(44) Sun, S.; Wei, L.; Li, Z.; Cao, G.; Liu, Y.; Lu, W. J.; Sun, Y. P.; Tian, H.; Yang, H.; Li, J. Direct Observation of an Optically Induced Charge Density Wave Transition In1T−$TaSe_2$. *Phys. Rev. B: Condens. Matter Mater. Phys.* **2015**, *92*, 224303.
(45) Golberg, D.; Bai, X. D.; Mitome, M.; Tang, C. C.; Zhi, C. Y.; Bando, Y. Structural Peculiarities of *In Situ* Deformation of a Multi-Walled BN Nanotube inside a High-Resolution Analytical Transmission Electron Microscope. *Acta Mater.* **2007**, *55*, 1293−1298.
(46) Stöger-Pollach, M. Optical Properties and Bandgaps from Low Loss Eels: Pitfalls and Solutions. *Micron* **2008**, *39*, 1092−1110.

DOI: 10.1021/acsnano.9b05466
ACS Nano 2019, 13, 11623−11631